

Supplementary Information for:

Near-surface Defects Break Symmetry in Water Adsorption on

$\text{CeO}_{2-x}(111)$

Oscar Custance^{1*†}, Manuel González Lastre^{2†}, Kyungmin Kim³,
Estefanía Fernández -Villanueva^{2,4,5}, Pablo Pou^{2,6}, Masayuki Abe³,
Hossein Sepehri-Amin¹, Shigeki Kawai¹, M. Verónica Ganduglia-Pirovano⁴,
Ruben Perez^{2,6*}

¹National Institute for Materials Science (NIMS), 1-2-1 Sengen, Tsukuba, 305-0047, Ibaraki, Japan.

²Departamento de Física Teórica de la Materia Condensada, Universidad Autónoma de Madrid, 28049, Madrid, Spain.

³Graduate School of Engineering Science, Osaka University, 1-3 Machikaneyama, Toyonaka, 560-0043, Osaka, Japan.

⁴Instituto de Catálisis y Petroleoquímica (CSIC), 28049, Madrid, Spain.

⁵Universitat Politècnica de València, Camí de Vera s/n, 46022, Valencia, Spain.

⁶Condensed Matter Physics Center (IFIMAC), Universidad Autónoma de Madrid, 28049, Madrid, Spain.

*Corresponding author(s). E-mail(s): custance.oscar@nims.go.jp; ruben.perez@uam.es;

[†]These authors contributed equally to this work.

Additional experimental figures

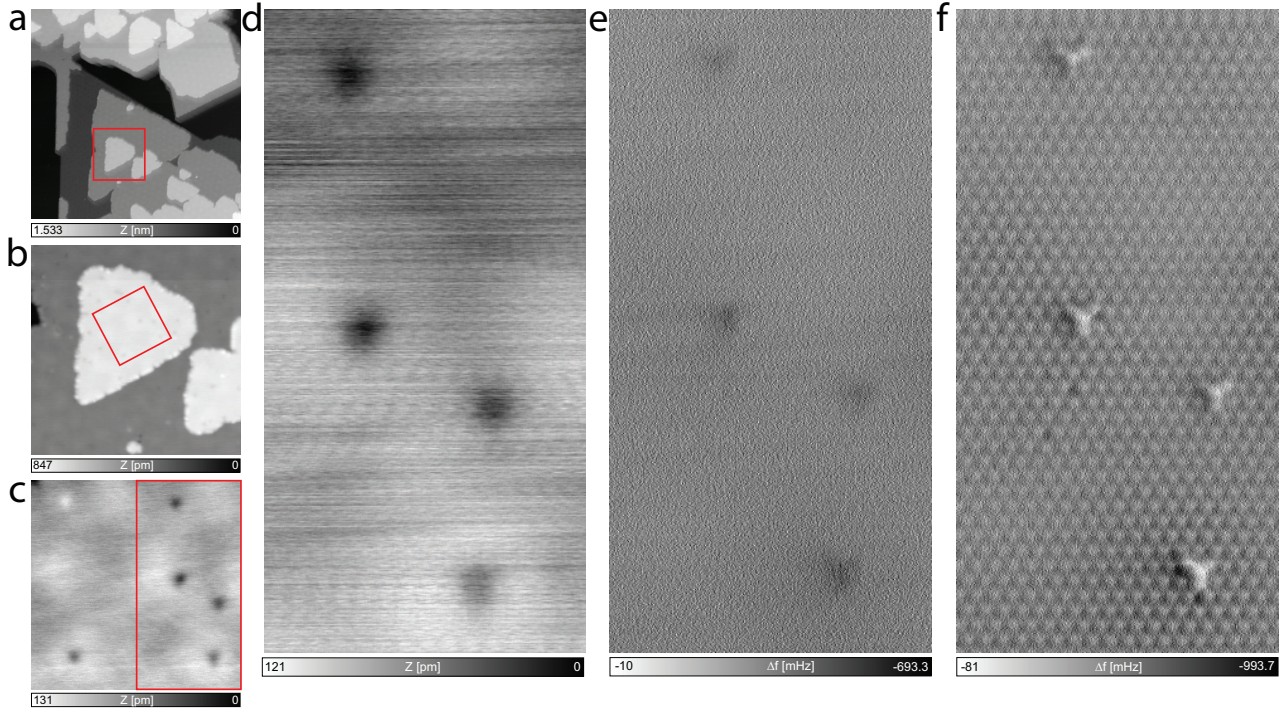


Fig. S1 Surface overview and water molecules location. (a) Topographic STM image of the surface area explored in these experiments. Size is (200×200) nm². (b) Topographic STM image of the CeO₂(111) island enclosed by a square in (a). Size is (50×50) nm². (c) Topographic STM image of the surface terraces highlighted by a rectangle in (b). Size is (15×15) nm². (d) Topographic STM image of the surface area displayed in Fig. 1a. (e) Constant-height AFM image at the probe-surface separation defined by the topographic set point in (d). (f) AFM image displayed in Fig. 1a. In these experiments, we used a sample bias voltage (V) of 2.5 V and tunneling current set point (I_{set}) of 2 pA for STM topographic imaging, an oscillation amplitude (A) of 60 pm and the sensor free oscillation resonant frequency (f_0) was 994230 Hz.

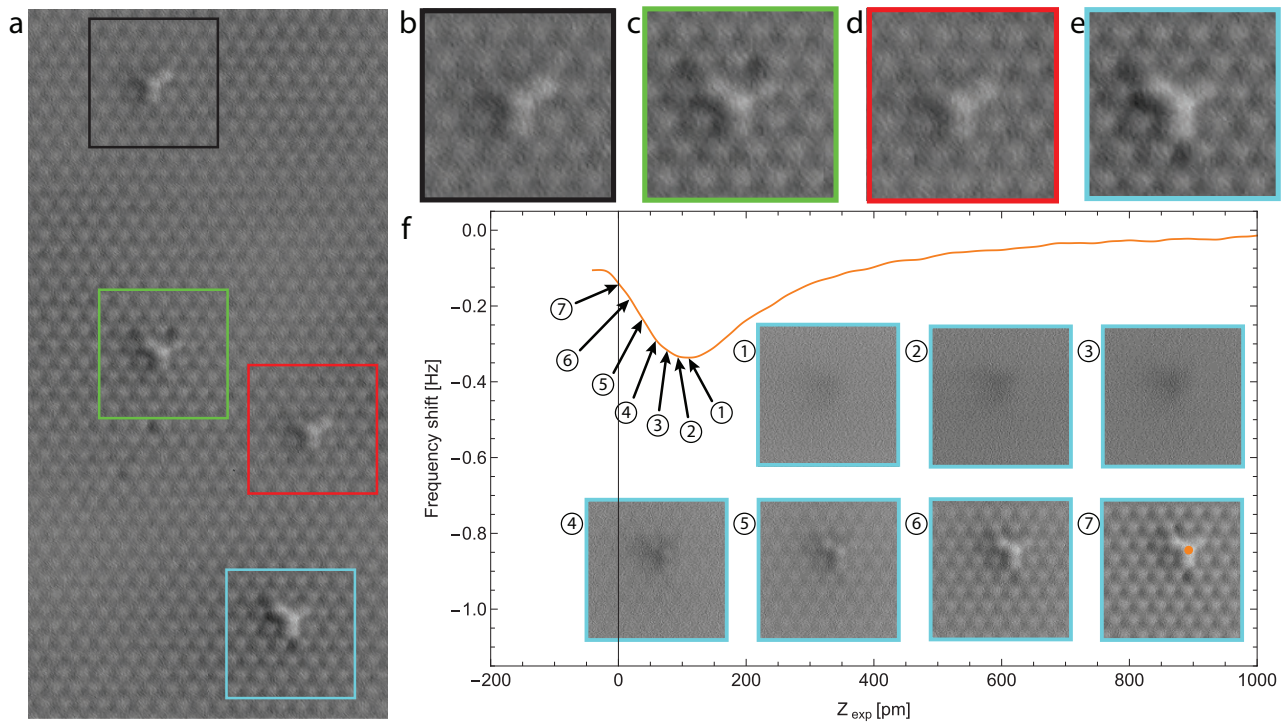


Fig. S2 AFM contrast of the water molecule. (a) Constant-height AFM image acquired several hours after the one displayed in Fig. 1a, in the same location and with the same acquisition parameters. The four water molecules appearing in the image have been enclosed by squares to label each molecule. (b) to (e) Detailed view of the water molecules appearing in (a). The color of the image frame in each panel matches the color of the squares in (a). The boomerang-like shape of the molecules appear on the right for (b) and (d), and on the left for (c) and (e). Notice that the boomerang-like shape orientation of the molecule in (b) changed from being oriented towards the top in Fig. 1a. to being oriented to right in (a). These observations exclude a probe artifact as the origin of the boomerang-like shape of the molecules. (f) Graph showing the AFM signal with the probe-surface distance measured at the center of the water molecule displayed in (e). The inset shows the variation of the AFM contrast over the water molecule in (e) with the probe-surface separation. **1** to **7** present constant-height AFM images acquired successively approaching the probe towards the surface from a distance at which some AFM signal over the molecule is detected (**1**) to the separation at which the image in (a) was obtained (**7**). The point in the force spectroscopy curve at which each image was measured is indicated by arrows labeled with the same number as the images.

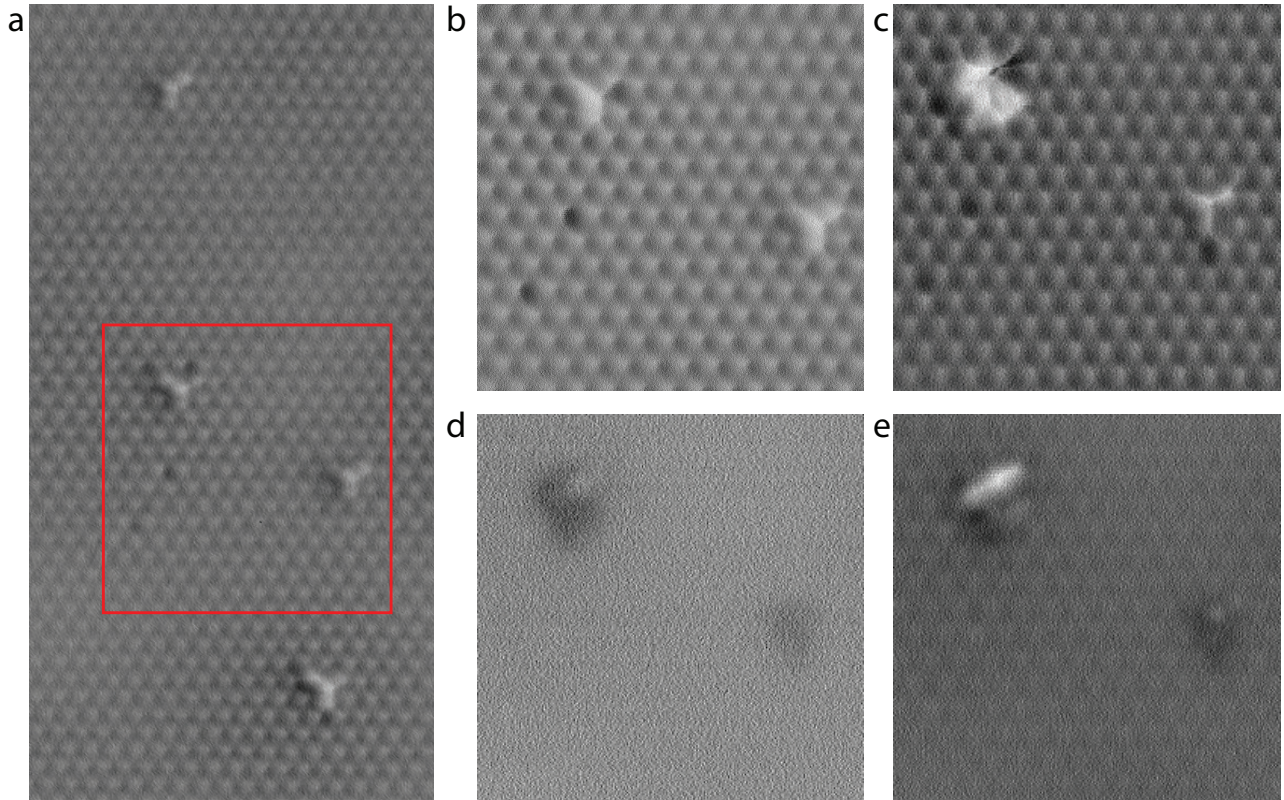


Fig. S3 Water lateral manipulation attempt. (a) AFM image displayed in Fig. S2a. (b) Constant-height AFM image of the region highlighted in (a). After taking this image we attempted the lateral manipulation of the water molecule shown in the upper left part of the image to a neighboring Ce site following the procedure we reported in *Nat. Mater.* **4**, 156 (2005) (DOI: 10.1038/nmat1297) that successfully enabled us to manipulate individual water molecules on the (111) surface of CeO_2 single crystals as reported in *J. Phys.: Condens. Matter.* **24**, 084010 (2012) (DOI: 10.1088/0953-8984/24/8/084010). However, we were unable to induce the jump of the water molecule even considerably increasing the probe-surface interaction. Instead of manipulating the water molecule, we induced the modification of the probe-surface interface. (c) Constant-height AFM image of the region highlighted in (a) after the manipulation attempt acquired at the same height as for (b). (d) and (e) Constant-height AFM image of the region highlighted in (a) retracting the probe by 173 pm and 114 pm, respectively, from the height the image in (c) was measured.

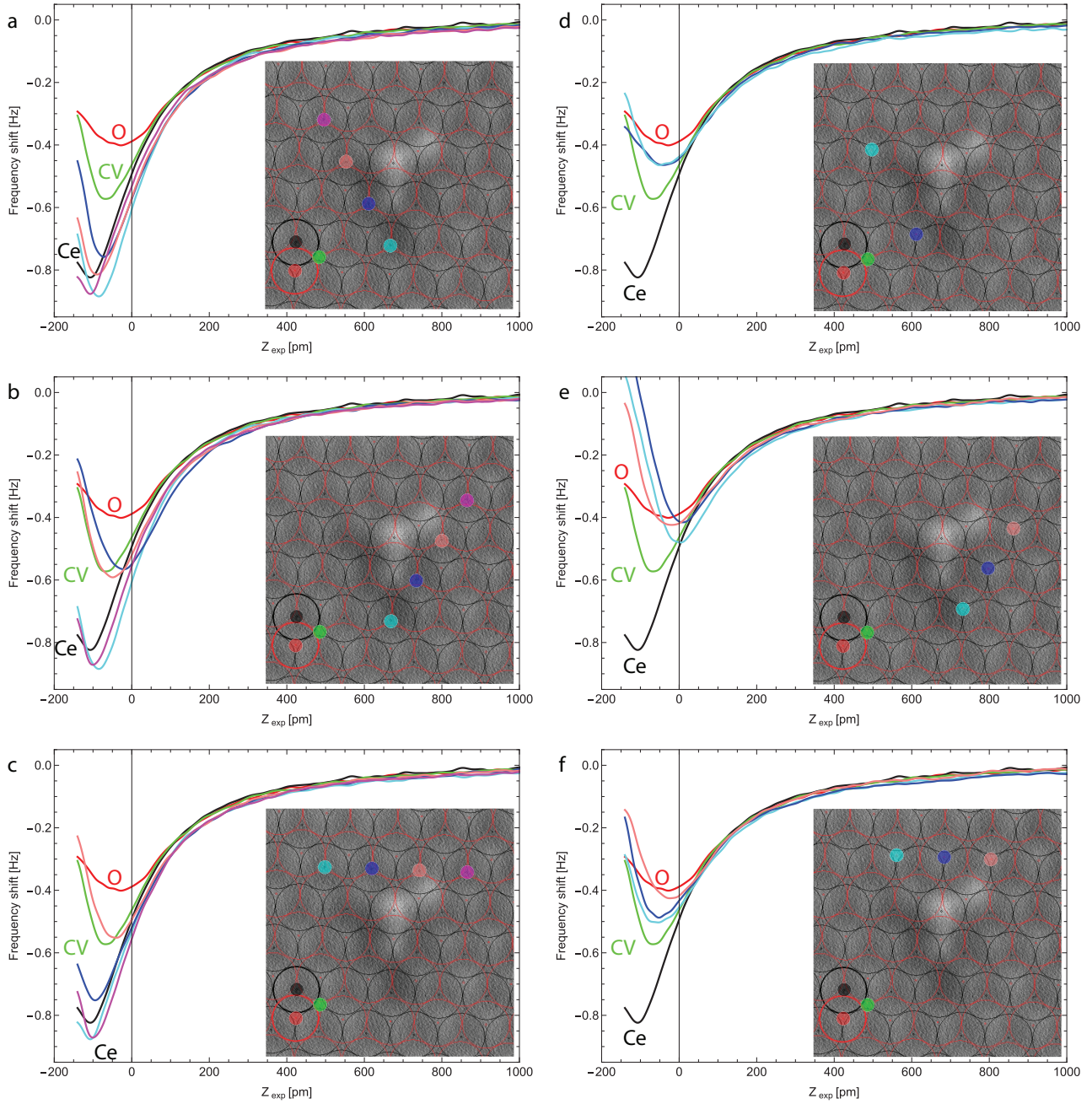


Fig. S4 Analysis of the force spectroscopy measurements displayed in Fig. 7. (a–c) Spectra acquired above Ce sites on the left, right, and top of the water molecule. (d–f) Spectra acquired above O sites in the same positions. In all the panels, curves measured over the three surface sites of the $\text{CeO}_2(111)$ surface (Ce in black, O in red and coordination vacancy in green) far from the water molecule are included for comparison. Color of the curves matches the color of the circles indicating the acquisition position in the inset image. A constant height AFM image measured before the spectroscopic acquisition is included in each panel. The black and red lattices superimposed to the image highlight the cerium and oxygen surface positions, respectively. The origin in the distance axis indicates the probe-surface separation the image was acquired.

Additional information for DFT calculations on water adsorption and dissociation

Calculations on the 3×3 unit cell

As discussed in the main text, the existence of a SSO_V and the corresponding Ce^{3+} changes the surface geometry and breaks its threefold symmetry, resulting in inequivalent sites for H_2O adsorption. In agreement with previous studies (Ref. 30 in the main text), the water molecule rarely stabilizes forming two hydrogen bonds with the surface oxygen atoms (structures **9**, **14** and **18** in Fig. S5). Instead, it prefers to form one hydrogen bond with an oxygen atom of the surface while the second hydrogen atom moves upwards, forming an angle of $\sim 120^\circ$ with the surface (e.g. structure **3** in Fig. S5). Since each cerium atom is surrounded by three surface oxygen atoms, the water molecule can form up to three different hydrogen bonds, and given that the free hydrogen atom can also be oriented to either side of this hydrogen bond (e.g. see structures **10** and **11** in Fig. S5), ultimately there are up to six different adsorption structure possibilities for the water molecule per cerium site (Fig. S5).

The geometric distortion of the surface due to the SSO_V is stronger for the sites surrounding it and for the Ce^{3+} sites, which is reflected in a greater adsorption energy change. In general, we found that the water molecule feels repulsion from the surface oxygen atoms, so that the closer they are, the less stable the adsorbed molecule becomes. As a result, adsorption energies correlate with the Ce-O bond distances of the cerium atom the water molecule adsorbs on.

More specifically, in the vicinity of the SSO_V the oxygen atoms move deeper into the surface as well as towards the vacancy, which causes the shortening of the two bonds adjacent to the SSO_V (~ 2.29 Å vs. 2.37 Å in the fully oxidized surface, see oxygen atom **A** in Fig. S14a). As a consequence, adsorptions at the Ce^{4+} neighboring the vacancy are the weakest ($+0.13$ eV, i.e. less exothermic), and among the possibilities, the molecule prefers to form the hydrogen bond with the oxygen atom that is furthest from the SSO_V . Meanwhile, Ce^{3+} ions are bigger than Ce^{4+} , and their Ce-O equilibrium distances are noticeably longer (2.46 - 2.64 Å, Ce^{3+} in green in Fig. S14a). This geometric effect compensates for the excess charge of the cerium atom (which in principle should lead to a greater repulsion with the water molecule) and actually leads to the strongest adsorption found.

Naturally, bond changes are amplified for those oxygen atoms that neighbor both the vacancy and the Ce^{3+} . In this case, the larger size of Ce^{3+} pushes the oxygen atoms even more toward the vacancy, further increasing the shortening effect by -0.04 Å and the elongating effect by 0.14 Å (~ 2.25 Å and ~ 2.64 Å, respectively, for the oxygen atoms **B** in Fig. S14a). Finally, the bond distances and energies obtained on the Ce^{4+} far from the vacancy are similar to the ones of the fully oxidized $\text{CeO}_2(111)$ surface, with the energy progressively getting less favorable as the cerium site approaches the location of the vacancy (Figs. S5c-e and Fig. S14a).

All in all, the adsorption energies and Ce-O bond distances for the different cerium sites follow the trend (Figs. S14a and S5): Ce^{3+} , with $\Delta E_{\text{ads}} \approx -0.79$ eV and $r_{\text{Ce-O}} \approx 2.46$ - 2.64 Å, binds more strongly than Ce^{4+} atoms far from the SSO_V ($\Delta E_{\text{ads}} \approx -0.72$ eV, $r_{\text{Ce-O}} \approx 2.30$ - 2.50 Å), which in turn bind more strongly than Ce^{4+} atoms close to the SSO_V ($\Delta E_{\text{ads}} \approx -0.66$ eV, $r_{\text{Ce-O}} \approx 2.25$ - 2.27 Å).

Calculations on the 4×4 unit cell

To ensure that our results on the stability of water on the Ce^{3+} , either in molecular or dissociated species (Fig. S6), were not significantly affected by the two Ce^{3+} atoms being neighbors on the (3×3) slab, we also calculated the crucial structures on the reduced $\text{CeO}_2(111)$ surface using a (4×4) model (Figs. S7a and S8b). Then, we also tested whether these results would qualitatively hold when the two Ce^{3+} atoms produced by the SSO_V are in the second energetically most stable configuration reported instead (see Ref. 63 in the main text), which is that of Ce^{3+} atoms labeled **11** and **13** in Fig. S14d (Figs. S7b and c and S8c and d, respectively).

We found no qualitative differences employing the former: the six water adsorption configurations follow the same trend in relative energies as for the calculations using the (3×3) slab (Figs. S5f and S7a), and again the $\text{OH} + \text{H}$ dissociated structure for the least stable configuration cannot be stabilized (**38** in Fig. S8). With the (4×4) surface, the Ce^{3+} atoms have more space to expand, which is reflected in small variations of the Ce-O distances with respect to the (3×3) slab: 2.672Å, 2.494Å and 2.512Å for the (4×4), and 2.642Å, 2.457Å and 2.537Å for the (3×3) (Figs. S14a and c). Nevertheless, the adsorption energies for the water molecule only vary within 0.03 eV (Fig. S7).

Regarding the second most stable (4×4) model, note that the Ce^{3+} atom labelled **11** is in the same position with respect to the vacancy as the Ce^{3+} atoms previously discussed, but the new location of the second Ce^{3+} atom (labeled **13**) causes large modifications to the Ce-O bond distances (Fig. S14d). The more dramatic change is for oxygen atom **B'** in Fig. S14d, which moves towards the SSO_V to a great extent, leading to a Ce-O bond that is substantially longer (2.854Å vs 2.671Å, Figs. S14c and d). As a consequence, adsorption energies on Ce^{3+} **11** are even higher than on the other Ce^{3+} configuration (Fig. S7c vs. Fig. S7a). Also, note that the adsorption energy for a water molecule forming a hydrogen bond with the surface oxygen atom **B'**, which neighbors the SSO_V , is no longer the less stable adsorption structure, but the most stable one, due to this dramatic Ce-O bond increase (-0.82 eV for structure **42** in Fig. S7c vs. -0.71 eV for structures **38** and **39** in Fig. S7a). In spite of this, we were still unable to generate a stable dissociated $\text{OH} + \text{H}$ structure from structure **42** in Fig. S7c, and thus the Ce^{3+} **11** site remains qualitatively similar to the Ce^{3+} in the previous configurations (Figs. S14a and c).

Regarding the Ce^{3+} atom labeled **13**, which neighbors the SSO_V , we found that its Ce-O bond distances are shorter than for any of the other Ce^{3+} atoms presented in this work (2.36-2.46Å, Fig. S14d). In fact, these bond distances are the result of a compromise between the larger size of Ce^{3+} , which is more stable with larger Ce-O distances, and the oxygen atoms **A'**, which are more stable toward the vacancy, i.e., with smaller Ce-O distances. As a result of these constrained Ce-O bond distances for a Ce^{3+} , adsorption energies are lower (about -0.69 eV). Finally, we tested several $\text{OH} + \text{H}$ structures at the Ce^{3+} atom **13**, but they produced even higher energies than for the water adsorption in molecular form, so we concluded that adsorption at this Ce^{3+} would not significantly contribute to the experimental measurements.

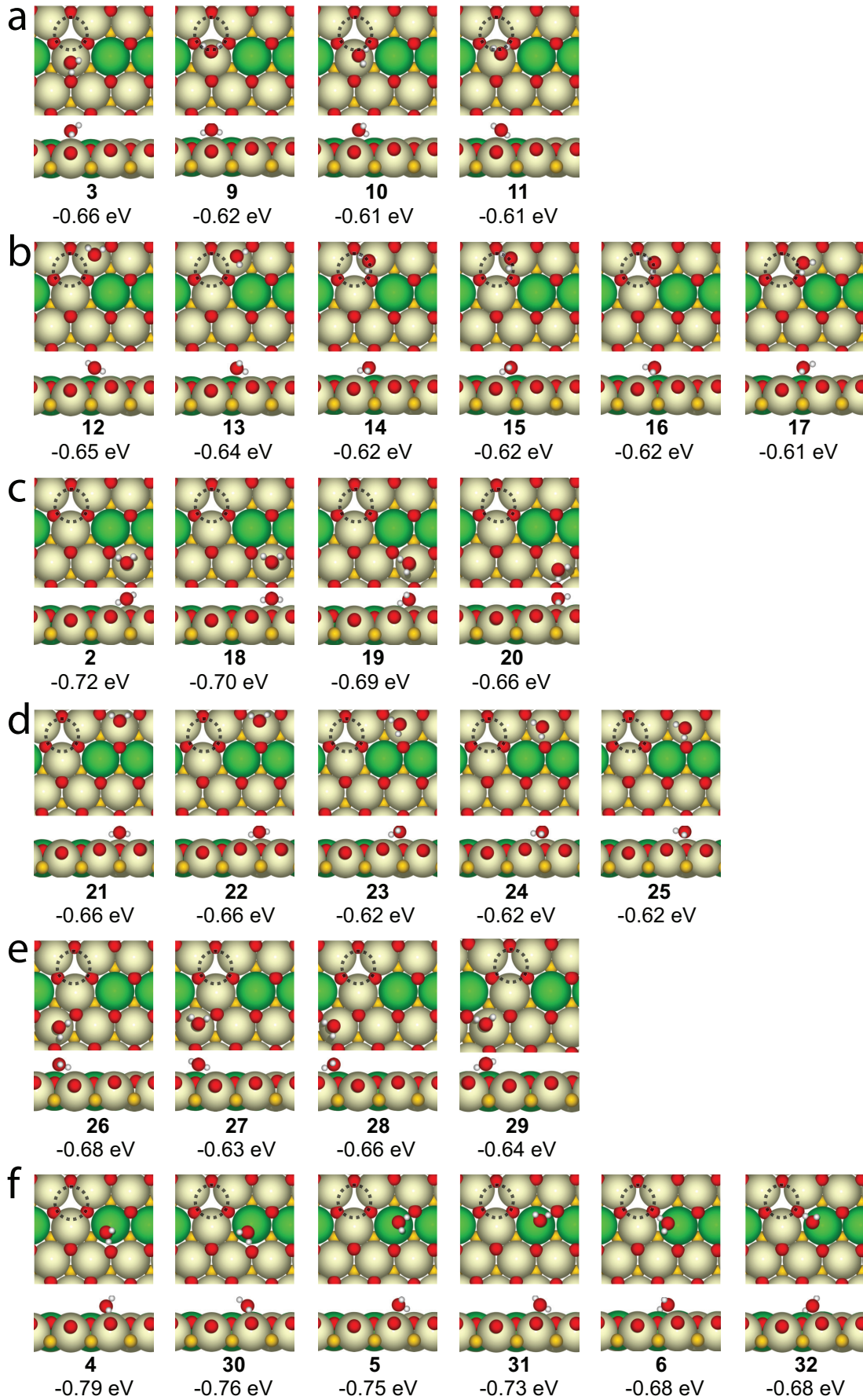


Fig. S5 DFT optimized water adsorption structures in the presence of a subsurface oxygen vacancy using a (3×3) unit cell. Calculated structures and energies for the adsorption of a water molecule at nonequivalent cerium sites of the $\text{CeO}_2(111)$ surface. The energetically most stable configuration for the position of the Ce^{3+} atoms generated by the subsurface oxygen vacancy was considered (see Ref. 61 in the main text). (a) and (b) Adsorption on nonequivalent Ce^{4+} atoms close to the vacancy. (c) to (e) Adsorption on nonequivalent Ce^{4+} far from the vacancy. (f) Adsorption on one of the two equivalent Ce^{3+} atoms of the structure. The energies with respect to the slab + water molecule are indicated under each structure. The position of the subsurface oxygen vacancy is highlighted by a dotted circumference. Ce^{3+} , Ce^{4+} , surface oxygen atoms and subsurface oxygen atoms are represented in green, beige, red and yellow, respectively.

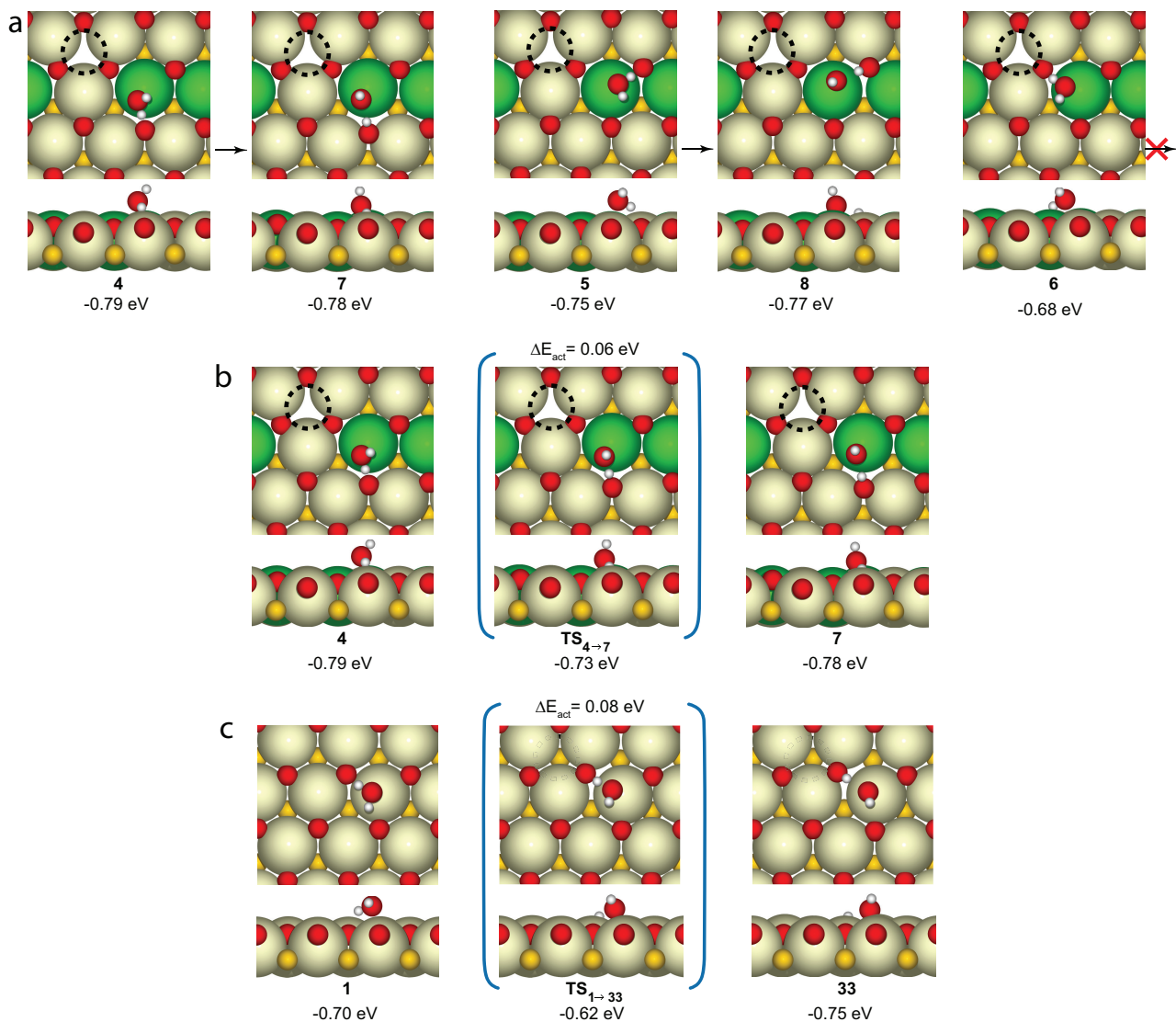


Fig. S6 DFT calculated dissociation and transition states of the water molecule using a (3×3) unit cell. (a) Molecular and dissociated water structures ($\text{H}_2\text{O} \rightarrow \text{OH} + \text{H}$) on the reduced $\text{CeO}_2(111)$ surface from Fig. 2 of the main text. (b) and (c) Water dissociation on the reduced and fully oxidized surface, respectively. The corresponding transition states (**TS**) structures and activation energies are shown within parenthesis. The energies with respect to the slab + water molecule are indicated under each structure. The position of the subsurface oxygen vacancy is highlighted by a dotted circumference. Ce^{3+} , Ce^{4+} , surface oxygen atoms and subsurface oxygen atoms are represented in green, beige, red and yellow, respectively.

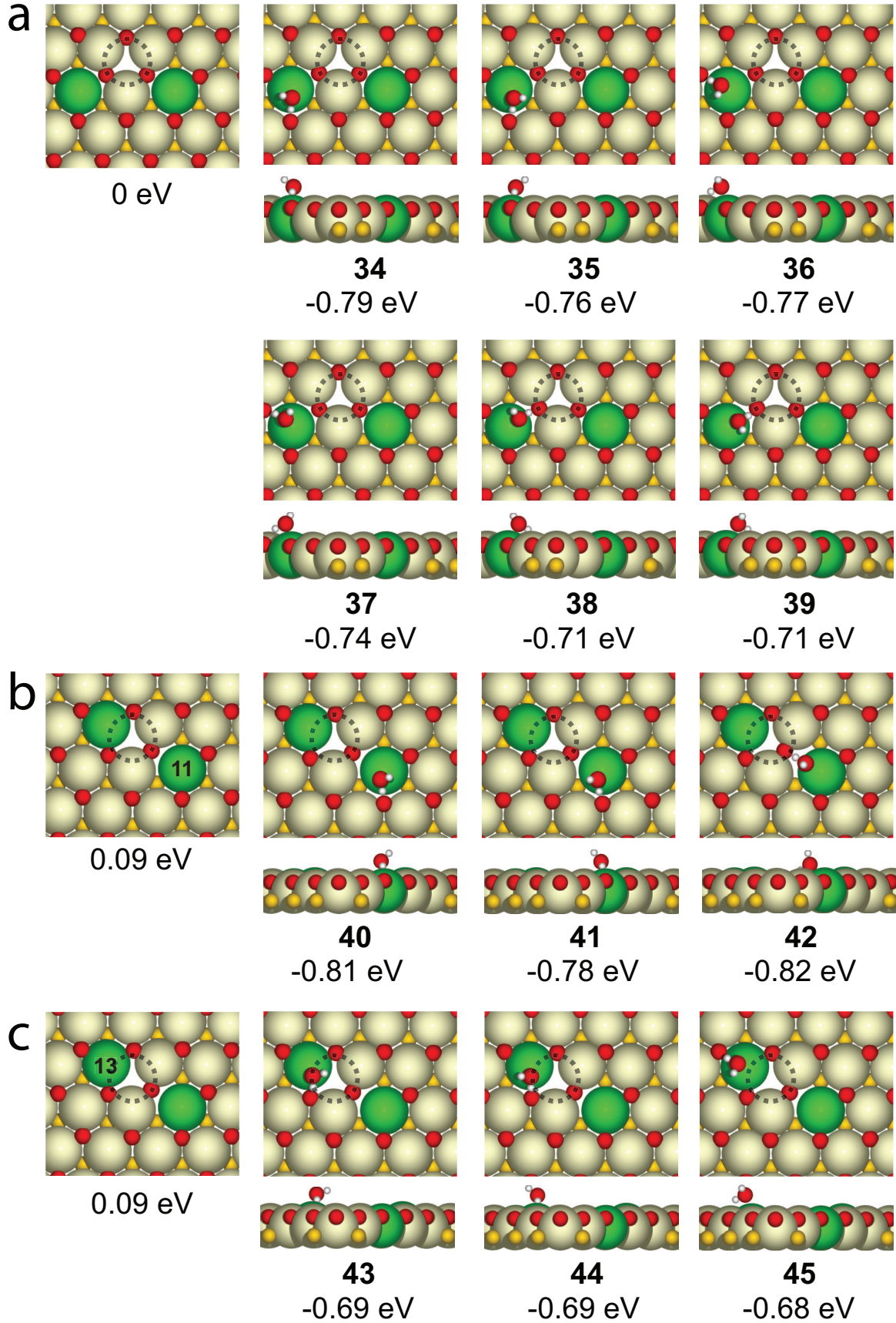


Fig. S7 DFT optimized structures for the water adsorption on nonequivalent Ce^{3+} atoms using a (4×4) unit cell. Structures for the water adsorption on each nonequivalent Ce^{3+} considering the most stable and second most stable positions for the Ce^{3+} atoms generated by the presence of a subsurface oxygen vacancy on the $\text{CeO}_2(111)$ surface. (a) Considering the energetically most stable configuration with the two Ce^{3+} atoms in equivalent positions. (b) and (c) Considering the energetically second most stable configuration with the two Ce^{3+} in nonequivalent positions. These Ce^{3+} atoms are labeled as **11** and **13** for reference. The energies with respect to the slab + water molecule are indicated under each structure. The position of the subsurface oxygen vacancy is highlighted by a dotted circumference. Ce^{3+} , Ce^{4+} , surface oxygen atoms and subsurface oxygen atoms are represented in green, beige, red and yellow, respectively.

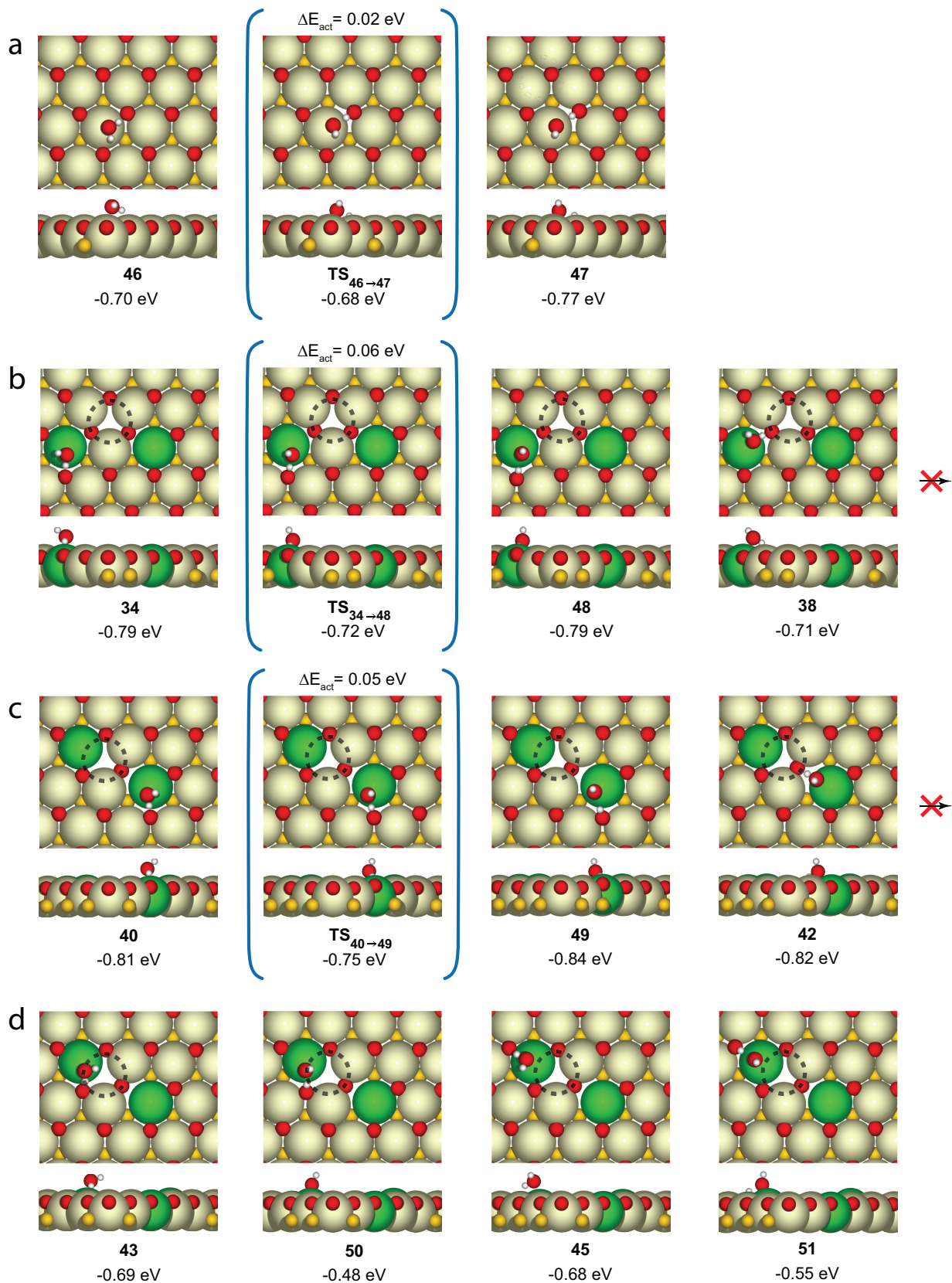


Fig. S8 DFT calculated dissociation and transition states of the water molecule using a (4×4) unit cell. Dissociated water ($\text{H}_2\text{O} \rightarrow \text{OH} + \text{H}$) and transition states (TS) structures and activation energies for: (a) a fully oxidized $\text{CeO}_2(111)$ surface; (b) a reduced surface considering the energetically most stable configuration for the position of the Ce^{3+} atoms; and (c) and (d) a reduced surface considering the second energetically most stable configuration for the position of the Ce^{3+} atoms, labeled as **11** and **13** in Figs. S14d and S7b and c. No OH + H stable configurations could be optimized from structures **38** and **42** from Fig.S7. The corresponding TS structures and activation energies are shown within parenthesis. No TS were calculated for (d) since the dissociated structures were significantly less stable than the molecular ones. The energies with respect to the slab + water molecule are indicated under each structure. The position of the subsurface oxygen vacancy is highlighted by a dotted circumference. Ce^{3+} , Ce^{4+} , surface oxygen atoms and subsurface oxygen atoms are represented in green, beige, red and yellow, respectively.

Additional information for simulations of AFM images and spectroscopy

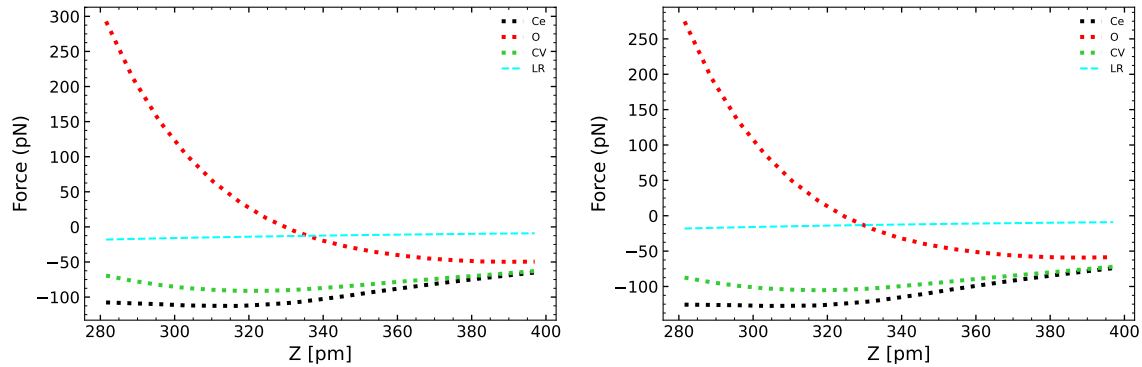


Fig. S9 Calculated force curves over a O (red), a Ce (black) and a CV (green) sites on a fully oxidized $\text{CeO}_2(111)$. Our model for the probe combines DFT forces with a CO molecule (left panel) with a long-range van der Waals contribution (cyan dashed curve), representing the macroscopic part of the probe, fitted to the experimental results at large distances and added to the DFT forces (right panel). These total forces are the ones used to calculate the frequency shift curves shown in Fig. 1 in the main text.

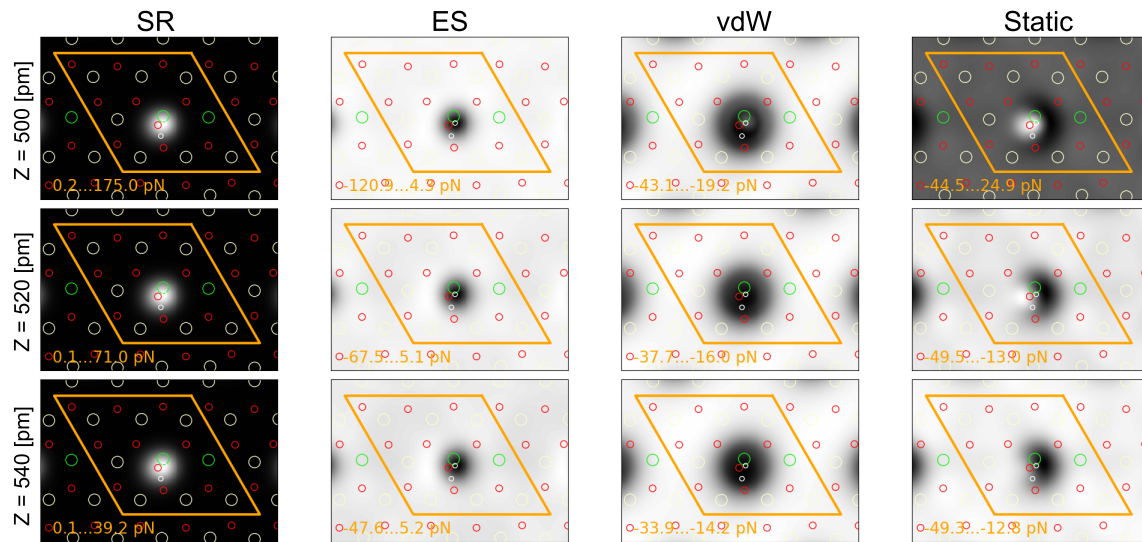


Fig. S10 Full Density Based Mode force decomposition for a water molecule adsorbed in molecular form over a Ce^{3+} . Decomposition of the AFM contrast obtained from Full Density-Based Model (FDBM) calculations for the water molecule in its molecular configuration adsorbed on a Ce^{3+} site of the reduced $\text{CeO}_2(111)$ surface (structure 4 in Fig. 2c). The total AFM signal (static) is split into short-range Pauli repulsion (SR), electrostatic (ES), and van der Waals (vdW) components. The brightest area for the total force image (static) corresponds to the highest contrast in the image displaying the Pauli repulsion (SR) only for the closest separation (500 pm). For larger separations, the electrostatic interaction (ES) also contributes to a degree in the calculated images. For the molecular adsorption configuration 5, the calculated Δf images (Fig. 3b), while presenting the same basic features discussed above, there are subtle contrast differences ultimately motivated by structural surface relaxations introduced by the presence of the vacancy and the associated Ce^{3+} ions.

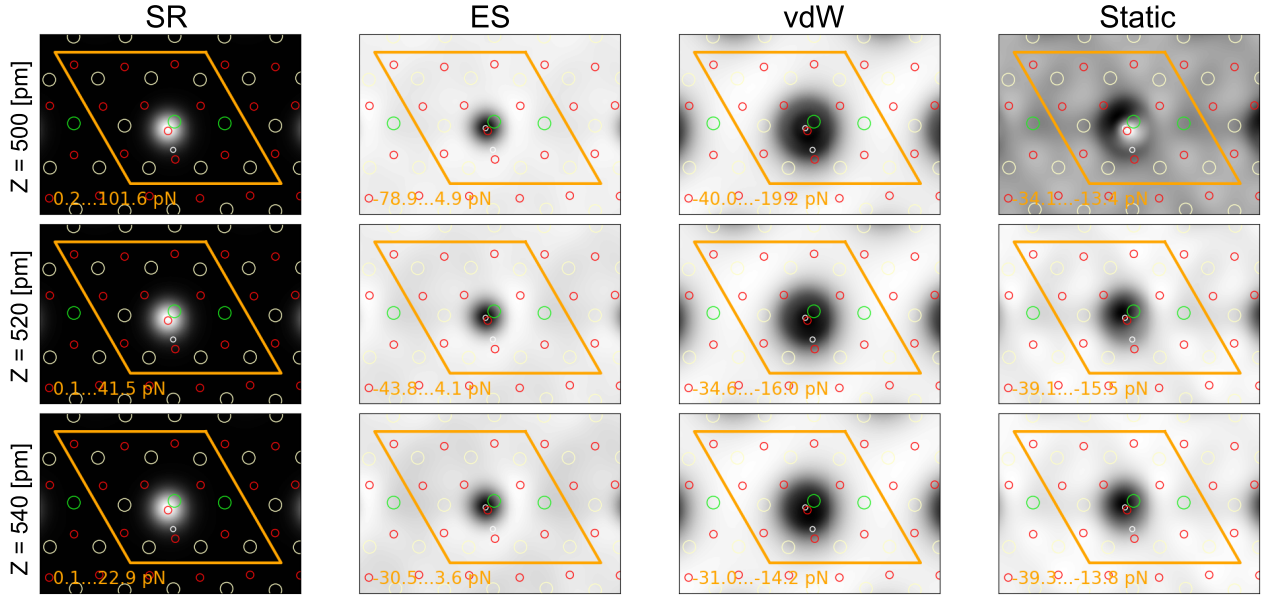


Fig. S11 Full Density Based Mode force decomposition for a water molecule adsorbed in dissociated form over a Ce^{3+} . Decomposition of the AFM contrast obtained from Full Density-Based Model (FDBM) calculations for the water molecule in its dissociated configuration ($\text{OH} + \text{H}$) adsorbed on a Ce^{3+} site of the reduced $\text{CeO}_2(111)$ surface (structure **7** in Fig. 2d).

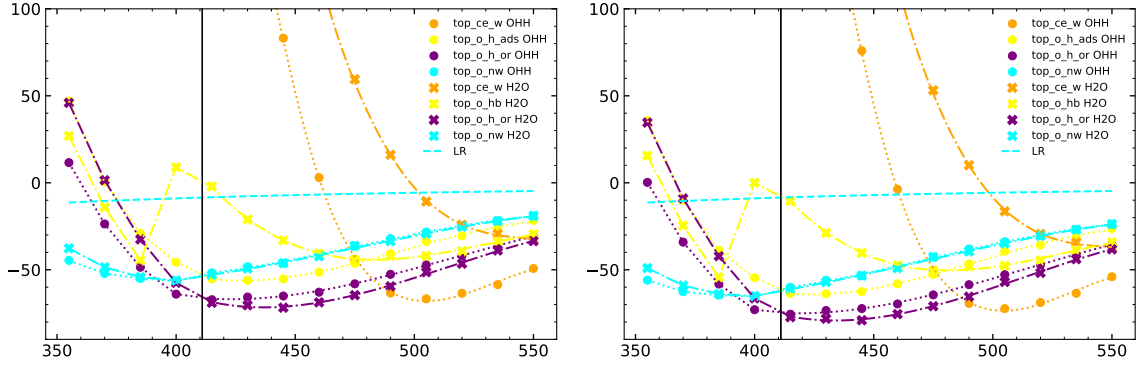


Fig. S12 Calculated force curves on different sites for water in molecular and hydroxyl pair states on a fully oxidized $\text{CeO}_2(111)$. Our model for the probe combines DFT forces with a CO molecule (left panel) with the long-range vdW contribution (cyan dashed curve), representing the macroscopic part of the probe, fitted to the experimental results at large distances and added to the DFT forces (right panel). These total forces are the ones used to calculate the frequency shift curves shown in Fig. 4 in the main text. We use the same color code to identify the sites

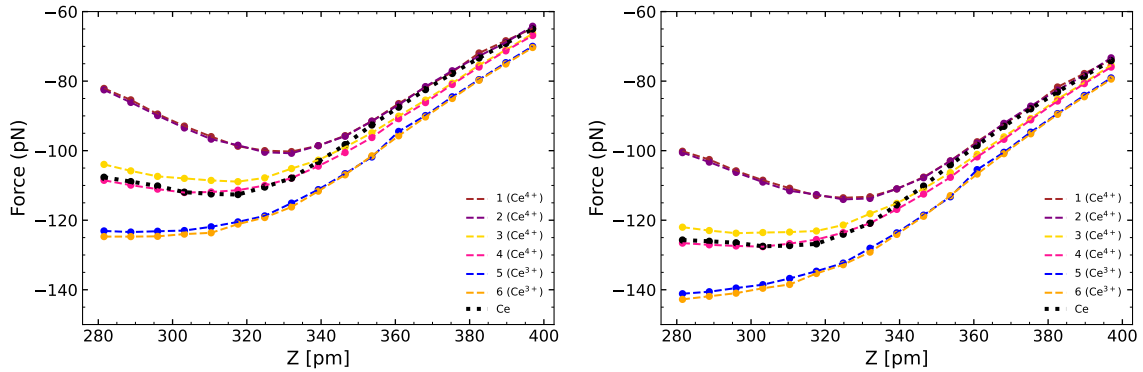


Fig. S13 Calculated force curves over different Ce sites close to an oxygen subsurface vacancy (SSO_V). Our model for the probe combines DFT forces with a CO molecule (left panel) with a long-range vdW contribution (not shown in the image), representing the macroscopic part of the probe, fitted to the experimental results at large distances and added to the DFT forces (right panel). These total forces are the ones used to calculate the frequency shift curves shown in Fig. 6 in the main text. We use the same numerical labels to identify the Ce sites: curves 1-4 correspond to Ce^{4+} ions and curves 5-6 to the Ce^{3+} ions in the reduced $\text{CeO}_{2-x}(111)$ surface shown as an inset in Fig. 6 of the main text.

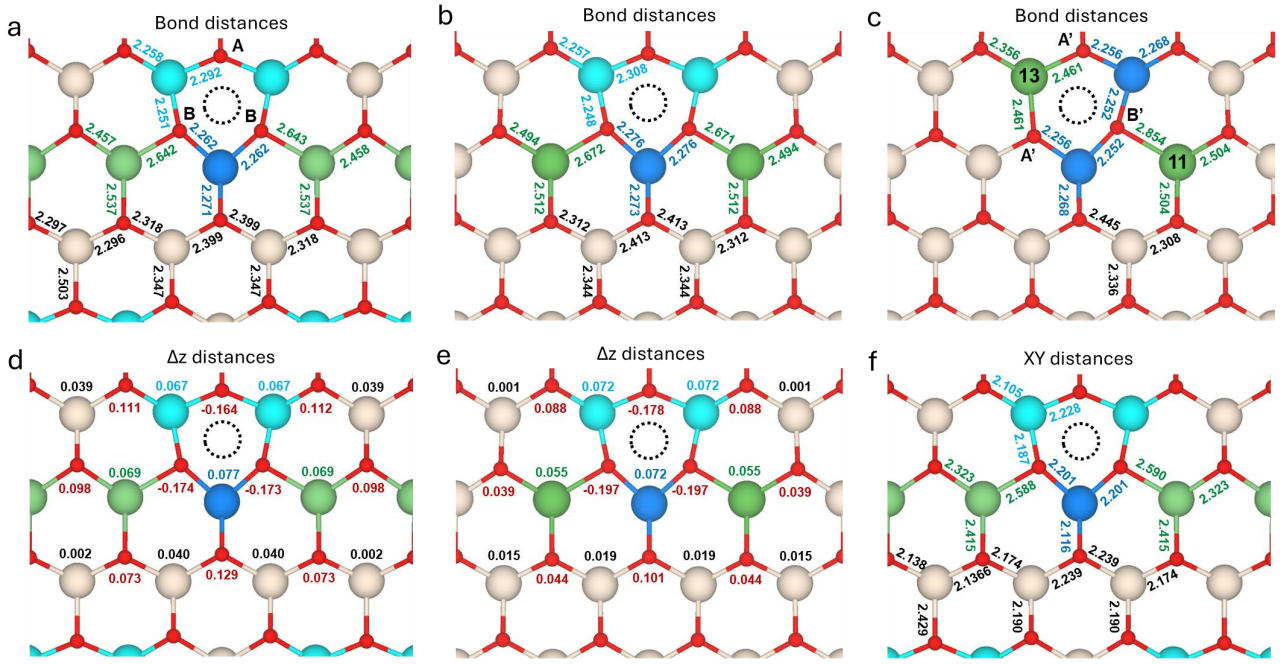


Fig. S14 Surface atomic relaxations near a subsurface oxygen vacancy. DFT optimized bond distances for the energetically most stable configuration of the two Ce^{3+} atoms produced by a subsurface oxygen vacancy (SSO_V) using a (3×3) slab (a) and the two most stable configurations using a (4×4) slab, (b) and (c). Difference in z (Δz) of the topmost Ce and O atoms with respect to the (3×3) and (4×4) clean surfaces, (d) and (e). Corresponding X-Y distances of the (3×3) structure are displayed in (f). All distances are indicated in Å. The bond distance on clean ceria is 2.369 Å. O vacancy marked with a dotted circle, Ce^{3+} atoms in green, Ce^{4+} atoms neighboring the SSO_V in blue (dark blue for the one that additionally neighbors the two Ce^{3+}), other Ce^{4+} in sand, surface O in red. Oxygen atoms neighboring the vacancy are also labeled for reference.

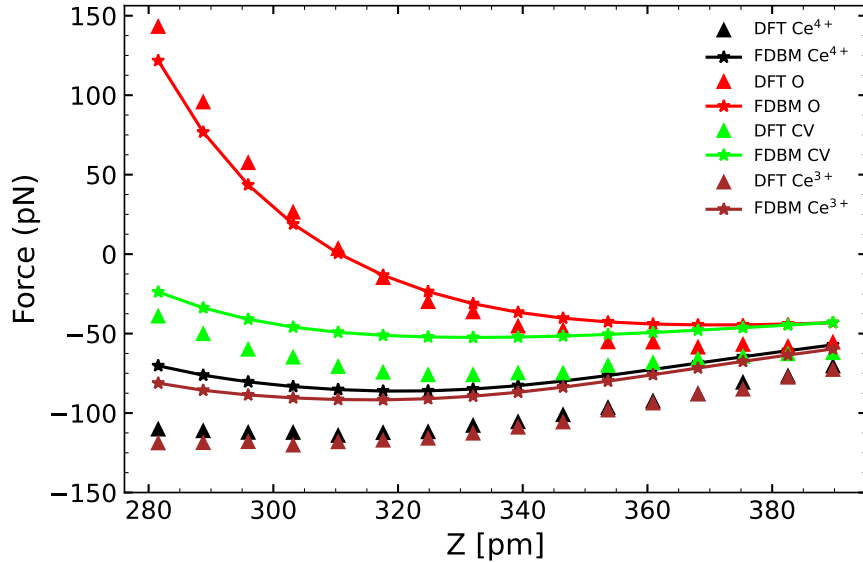


Fig. S15 Fitting of the Full Density Based Mode short-range parameters (α, V_0). DFT force-distance curves computed with a rigid CO probe (symbols) and fitted Full Density-Based Model (FDBM) forces (lines) over the reduced $\text{CeO}_{2-x}(111)$. The short-range FDBM parameters (α, V_0) are obtained by a least-squares fit of the total force (SR + ES + vdW_{D3}) to the DFT forces, obtaining $\alpha = 1.08$ and $V_0 = 36.96 \text{ eV/\AA}^{3(2\alpha-1)}$. With these values, the model should accurately describe the interaction with water molecules adsorbed on the $\text{CeO}_2(111)$ surface. Since the oxygen atom in the water molecule lies approximately $\sim 2 \text{ \AA}$ above the surface oxygens, images of water acquired at probe-surface distances around $\sim 5 \text{ \AA}$ should be well captured by the FDBM approach.

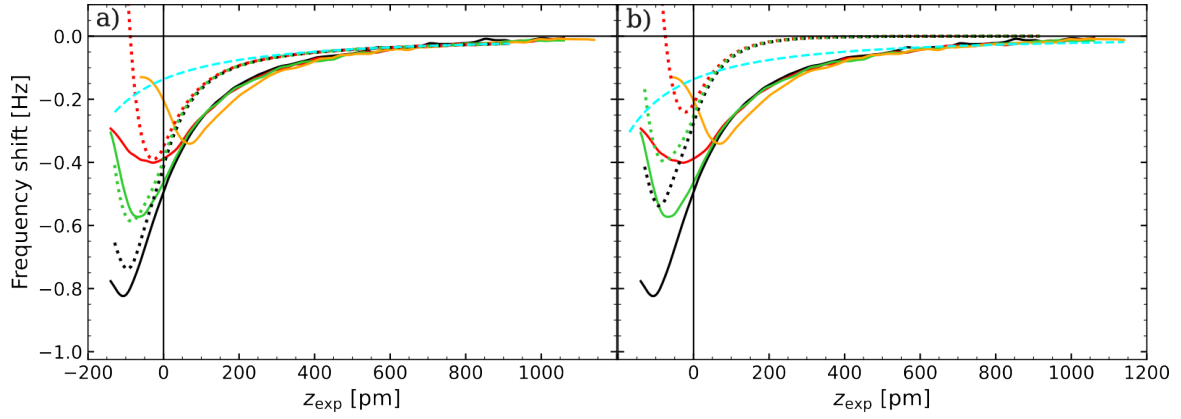


Fig. S16 Fitting the van der Waals (vdW) contribution of the mesoscopic part of the probe. Frequency shift (Δf) experimental and DFT curves measured at the top of the water molecule (orange), and on an O (red), a Ce (black) and a CV (green) with the long range vdW. Panel a) reproduces Fig. 1d where the long range vdW contribution has already been summed to the DFT curves. In b), this contribution is not added, so at large distances we recover the natural oscillation frequency. To be able to compare the ab initio simulations to the experiments, we fit the long-range tails of the experimental curves (the region at which all curves start converging, $z \in [400, 1140]$) to Eq. 2, yielding $C = -1.4311 \times 10^{-6} \text{ N pm}^2$.

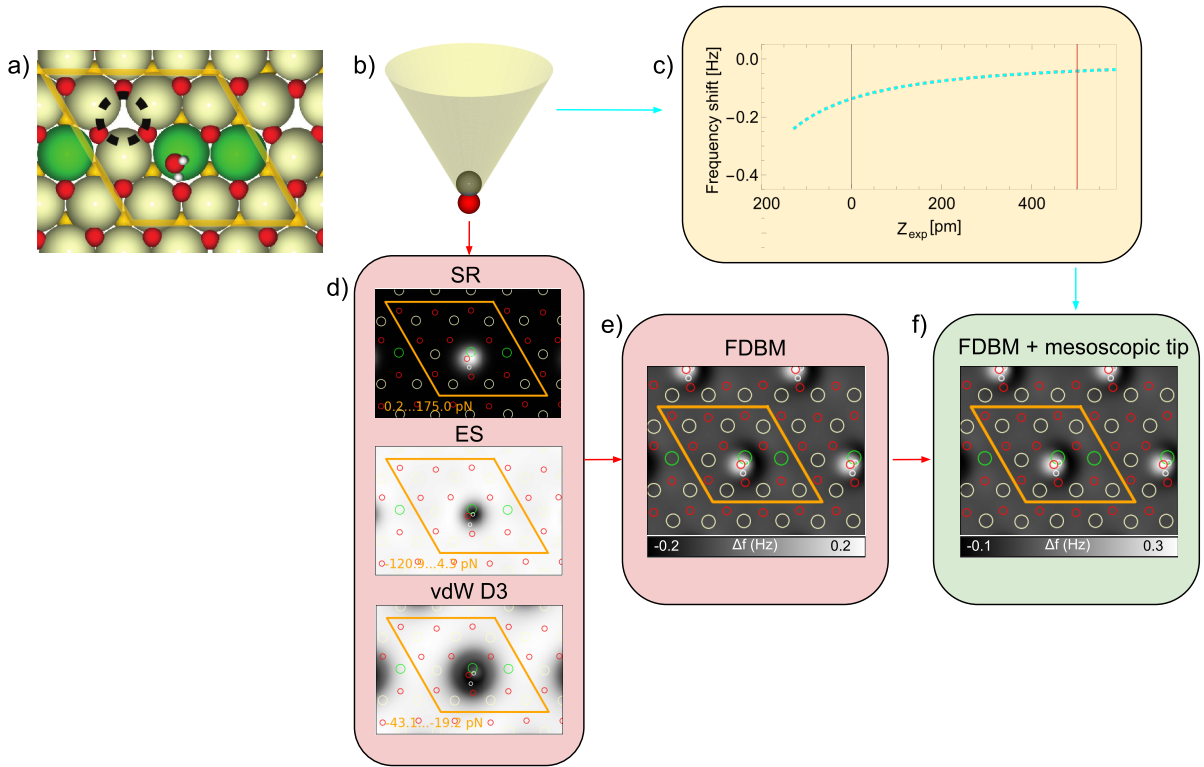


Fig. S17 Schematic workflow for the calculation of Δf images. (a) Molecular water adsorbed on CeO_{2-x} in configuration 4. (b) Model probe composed of a rigid CO molecule to represent the chemically sensitive apex, together with a mesoscopic probe (yellow cone) that contributes only a long-range van der Waals interaction (c) described by Eq. 2. (d) The interaction from the CO termination is described with the Full Density Based Mode (FDBM), which separates the forces into short-range Pauli repulsion (SR), electrostatic (ES), and van der Waals contributions obtained from the D3 method (vdW D3). (e) These contributions are combined to generate the total short-range force field and the corresponding Δf images. Finally, the long range vdW term—calibrated from the large-distance tail of the experimental $\Delta f(z)$ curves—is added to account for the mesoscopic part of the probe, providing the total simulated Δf maps used for comparison with experiment.

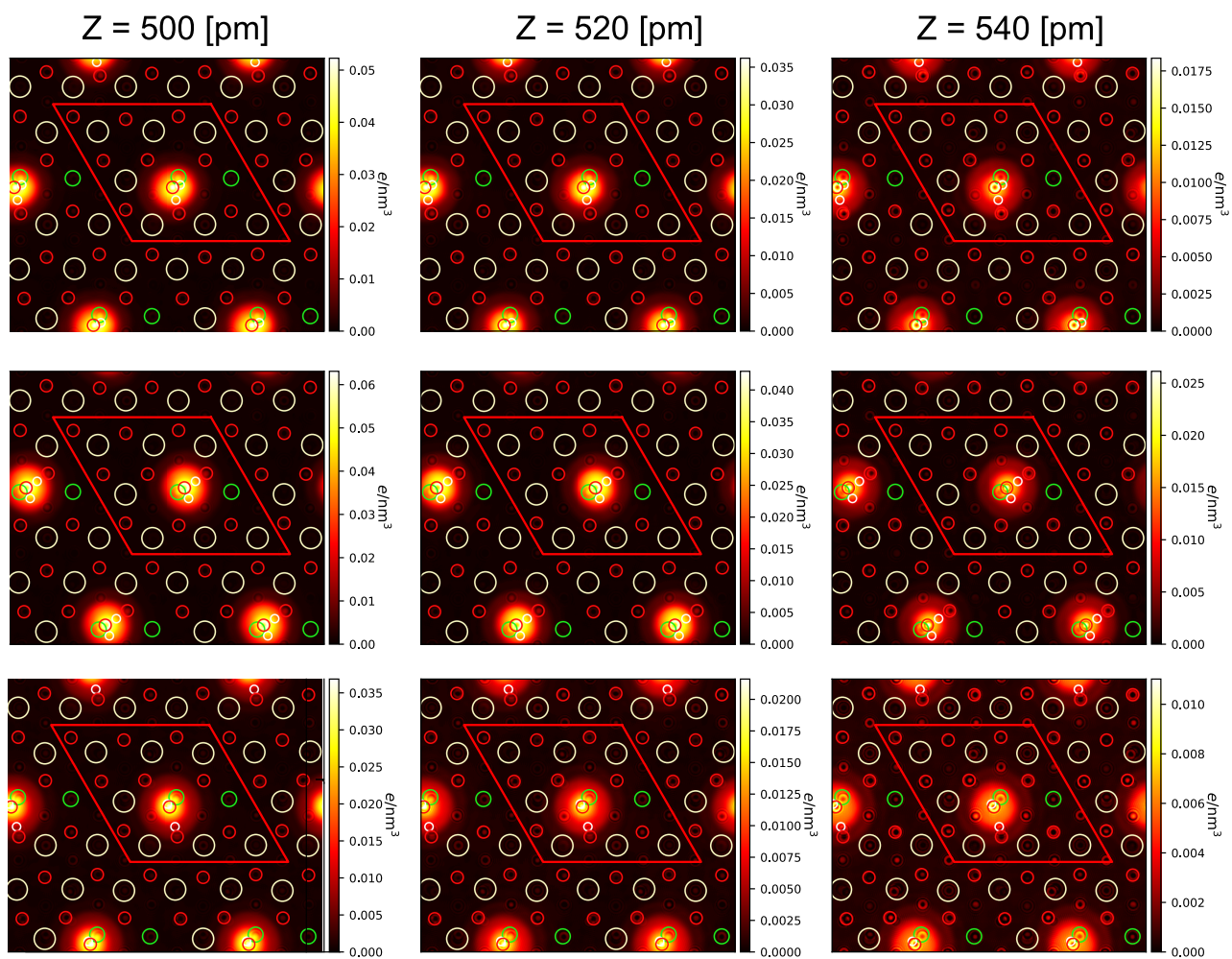


Fig. S18 DFT charge density for molecular and dissociated water adsorbed over a Ce^{3+} . Electronic charge density for the molecular and dissociated ($\text{OH} + \text{H}$) configurations adsorbed on a Ce^{3+} site of the reduced $\text{CeO}_2(111)$ surface depicted in Fig. 3. This charge density is used to compute the short-range repulsion in the Full Density Based Model (FDBM).

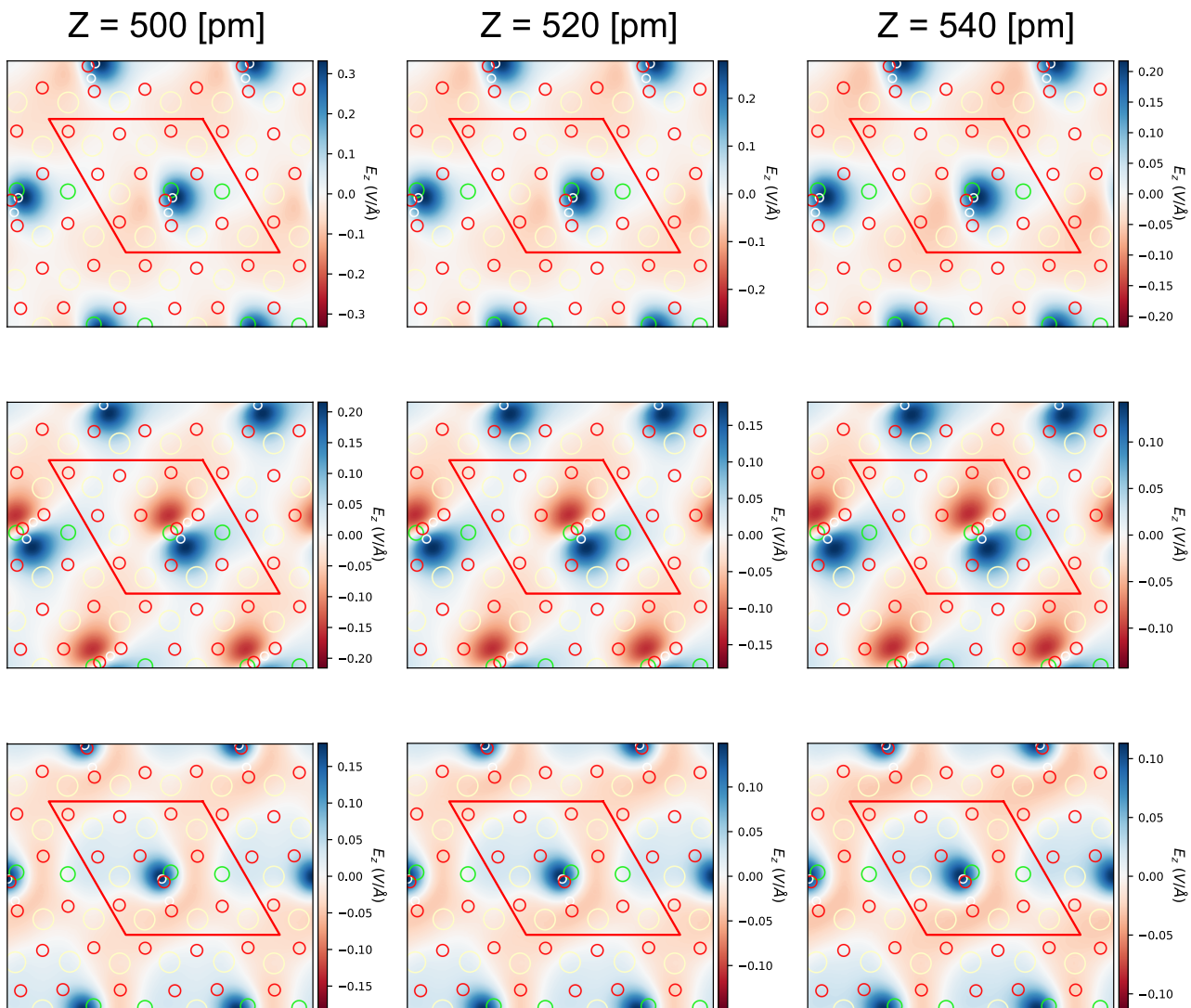


Fig. S19 Vertical electric field E_z for molecular and dissociated water adsorbed over a Ce^{3+} . E_z for the molecular and dissociated ($\text{OH} + \text{H}$) configurations adsorbed on a Ce^{3+} site of the reduced $\text{CeO}_2(111)$ surface depicted in Fig. 3. The Hartree potential from which we calculate the E_z is used to compute the electrostatic interaction in the Full Density Based Mode (FDBM).